PHYSICAL REVIEW A **92**, 053402 (2015)

Vibrational-coherence measurement of nonequilibrium quantum systems by four-wave mixing

Alexander Schubert,[1,*] Cyril Falvo,[2] and Christoph Meier[1]

[1] *Laboratoire Collisions Agrégats et Réactivité, IRSAMC, UMR CNRS 5589, Université Paul Sabatier, 31062 Toulouse, France*

[2] *Institut des Sciences Moléculaires d'Orsay (ISMO), CNRS, Univ. Paris-Sud, Université Paris-Saclay, 91405 Orsay, France*

(Received 19 June 2015; published 4 November 2015)

We show theoretically that a quantum system in a nonequilibrium state interacting with a set of laser pulses in a four-wave-mixing setup leads to signal emission in directions opposite to the ones usually considered. When combined with a pump mechanism which sets a time origin for the nonequilibrium state creation, this particular optical response can be utilized to directly follow decoherence processes in real time. By varying the time delays within the probe sequence, signals in these unconventional directions can also be used to detect two-dimensional spectra determined by the dynamics of up to three-quantum coherences, revealing energetical anharmonicities and environmental influences. As a numerical example, these findings are demonstrated by considering a model of vibrational decoherence of carbon monoxide after photolysis from a hemeprotein.

DOI: 10.1103/PhysRevA.92.053402   PACS number(s): 42.50.Md, 33.20.Tp, 78.47.nj, 82.53.−k

I. INTRODUCTION

Over the past decades, multidimensional spectroscopy has proven to be a unique tool to investigate structural and dynamical properties of complex molecular systems. Having its historical origins in two-dimensional (2D) NMR spectroscopy [1], the fundamental principle of time-delay modulated pulse sequences interacting with a sample has successfully been adapted to the infrared and visible regime [2–4], probing coherent vibrational and electronic dynamics on the femtosecond time scales. In such multidimensional spectroscopy experiments, the induced signals resulting from the interaction between the sample and the laser pulses are emitted in specific directions following the phase-matching condition, which gives rise to a vast number of experimental techniques [5–7]. This opened the way to investigate fundamental physical, chemical, and biochemical processes in the time domain [8–12]. In the context of transient species, multidimensional spectroscopy was also extended to analyze systems in a nonequilibrium state prior to the detection scheme [13–19]. In this case, a first pulse triggers a complex dynamical process, such as dissociation, internal conversion, or geometrical rearrangement, before the acquired quantum state is probed by a four-wave-mixing (FWM) pulse configuration (see Fig. 1). In such transient states, coherences may arise and the question, to what extent they affect the process, recently aroused strong interest in their theoretical and experimental investigation [20–28]. Just recently Agarwalla *et al.* showed that the optical response of nonequilibrium quantum systems, in which time-translational symmetry is broken, leads to new resonances in n-wave mixing [29].

In this general context, we show that the presence of coherences, created by an arbitrary preceding process, causes signal emission in phase-matching directions opposite to the ones traditionally used in FWM experiments. Since these signals are directly proportional to off-diagonal elements of the nonequilibrium density matrix, they allow for the direct, background-free observation of decoherence in real time. We use the example of a UV-2D-IR sequence and the detection of vibrational coherences, but the underlying principle is of a more general nature and applicable to all 2D spectroscopy techniques.

The article is organized as follows. In Sec. II, we briefly review the general theory of optical response and apply it to a nonequilibrium quantum system with vibrational coherences interacting with a sequence of three IR pulses. In a second step, we derive the appearance of emission signals if initial coherences are present. The findings are illustrated by numerical simulations of the carbon monoxide vibration, stemming from a dissociation from a hemeprotein by a preceding UV pulse. Details of the simulation are given in Sec. III. Results

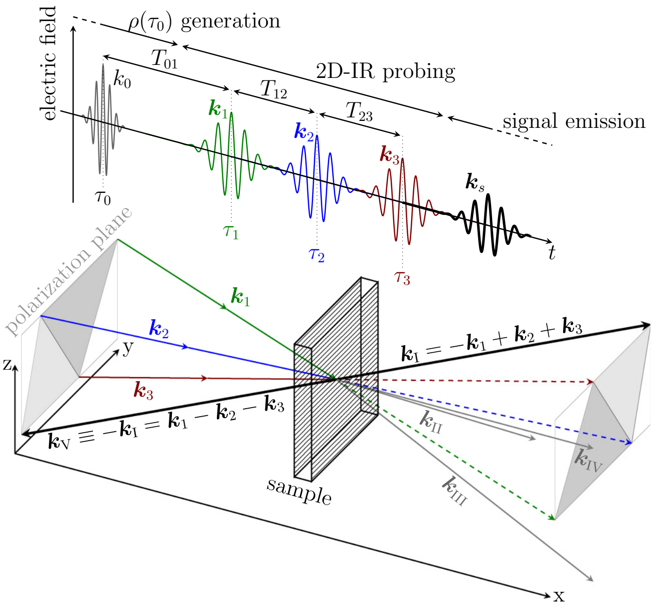

FIG. 1. (Color online) In transient 2D-IR spectroscopy, a pump pulse ($\boldsymbol{k}_0$) generates a nonequilibrium state $\rho(\tau_0)$, followed by a three-pulse probe sequence ($\boldsymbol{k}_1$,$\boldsymbol{k}_2$,$\boldsymbol{k}_3$) inducing a third-order polarization $\mathcal{P}_s^{(3)}(t)$, which leads to radiative emission in directions $\boldsymbol{k}_s$ according to the phase-matching condition. The presence of coherences causes emissions opposite to directions usually used in conventional detection schemes.

---

[*] schubert@irsamc.ups-tlse.fr

©2015 American Physical Society

comprising FWM and 2D-IR spectra in different detection directions are presented and analyzed in Sec. IV. A final conclusion and outlook is given in Sec. V.

II. THEORY

A. Third-order optical response of a system in a nonequilibrium state

We consider a quantum system expressed in its spectral decomposition $\hat{H}_0 = \sum_{n\geq 0} \epsilon_n |n\rangle\langle n|$, which we assume to be in a nonequilibrium state prior to the interaction with a sequence of three near-resonant IR pulses. The total electric field is given by $E_{\text{inc}}(\boldsymbol{r},t) = \mathcal{E}_{\text{inc}}(\boldsymbol{r},t) + \mathcal{E}^*_{\text{inc}}(\boldsymbol{r},t)$, where $\mathcal{E}_{\text{inc}}(\boldsymbol{r},t)$ is written as

$$\mathcal{E}_{\text{inc}}(\boldsymbol{r},t) = \sum_{p=1}^{3} \varepsilon_p(t-\tau_p)\, e^{i\boldsymbol{k}_p\boldsymbol{r} - i\omega_p(t-\tau_p)}, \tag{1}$$

and $\boldsymbol{k}_p, \omega_p, \tau_p$, and $\varepsilon_p(t)$ are the wave vector, frequency, center, and envelope of the different laser pulses, respectively.

Using the rotating wave approximation (RWA), the molecule-field interaction can be written as [30]

$$\hat{W}(\boldsymbol{r},t) = -\hat{V}\mathcal{E}^*_{\text{inc}}(\boldsymbol{r},t) - \hat{V}^{\dagger}\mathcal{E}_{\text{inc}}(\boldsymbol{r},t) \tag{2}$$

with $\hat{V} = \sum_{n\geq 0} \mu_{n,n+1}|n\rangle\langle n+1|$ inducing downward transitions on ket states.

Under these assumptions, the macroscopic polarization can be written as the sum of two conjugate contributions $P(\boldsymbol{r},t) = \mathcal{P}(\boldsymbol{r},t) + \mathcal{P}^*(\boldsymbol{r},t)$ with

$$\mathcal{P}(\boldsymbol{r},t) = \text{Tr}\{\hat{V}\rho(\boldsymbol{r},t)\}, \tag{3}$$

where $\rho(\boldsymbol{r},t)$ is the system density matrix [5]. With this definition, it is sufficient to analyze emission from ket states, which contribute to $\mathcal{P}$, whereas the corresponding emissions from bra states are comprised in $\mathcal{P}^*$.

Defining the Liouville superoperators $\mathcal{H}_0 = [\hat{H}_0, \cdot\,]$ and $\mathcal{W} = [\hat{W}, \cdot\,]$, and using the interaction representation

$$\begin{aligned} \mathcal{W}_I(\boldsymbol{r},t) =& e^{i\mathcal{H}_0(t-\tau_0)}\mathcal{W}(\boldsymbol{r},t)e^{-i\mathcal{H}_0(t-\tau_0)}, \\ \hat{V}_I(t) =& e^{i\hat{H}_0(t-\tau_0)}\hat{V}\, e^{-i\hat{H}_0(t-\tau_0)}, \end{aligned} \tag{4}$$

one can express $\mathcal{P}(\boldsymbol{r},t)$ within third-order perturbation theory as [29]

$$\begin{aligned} \mathcal{P}^{(3)}(\boldsymbol{r},t) = (-i)^3 \int_{\tau_0}^{t} dt_3 \int_{\tau_0}^{t_3} dt_2 \int_{\tau_0}^{t_2} dt_1\, \text{Tr}\{\hat{V}_I(t) \\ \times \mathcal{W}_I(\boldsymbol{r},t_3)\mathcal{W}_I(\boldsymbol{r},t_2)\mathcal{W}_I(\boldsymbol{r},t_1)\rho(\tau_0)\}. \end{aligned} \tag{5}$$

As stated above, we assume that the initial density matrix $\rho(\tau_0)$ represents a nonequilibrium state, including coherences. As such, it shows an explicit time dependence. In addition, we take $\rho(\tau_0)$ to be independent of $\boldsymbol{r}$, i.e., consider the systems to be spatially uniformly distributed. For example, this situation is encountered for vibrational coherences in electronically excited states created by a short UV pulse, as depicted in Fig. 1, and detailed in Appendix A.

Assuming that each laser pulse interacts with the system once and that the pulses do not overlap, the third-order polarization can be divided into eight contributions according to

$$\mathcal{P}^{(3)}(\boldsymbol{r},t) = \sum_{s=\text{I}}^{\text{VIII}} e^{i\boldsymbol{k}_s\boldsymbol{r}}\mathcal{P}^{(3)}_s(t), \tag{6}$$

separated by their spatial phase factors, containing the distinctive sign configuration of the wave vector $\boldsymbol{k}_s = \pm\boldsymbol{k}_1 \pm \boldsymbol{k}_2 \pm \boldsymbol{k}_3$ [5]. Here, $\mathcal{P}^{(3)}_s(t)$ is induced by a particular interaction sequence

$$\begin{aligned} \mathcal{P}^{(3)}_s(t) = -i \int_{\tau_0}^{t} dt_3 \int_{\tau_0}^{t_3} dt_2 \int_{\tau_0}^{t_2} dt_1 \\ \times \text{Tr}\Bigg\{ \prod_{p=1}^{3}(\varepsilon_p(t_p-\tau_p)e^{i\alpha^s_p\omega_p(t_p-\tau_p)}) \\ \times \hat{V}_I(t)\mathcal{V}_I^{s_3}(t_3)\mathcal{V}_I^{s_2}(t_2)\mathcal{V}_I^{s_1}(t_1)\rho(\tau_0)\Bigg\}, \end{aligned} \tag{7}$$

with the Liouvillian

$$\mathcal{V}_I^{(\dagger)}(t) = e^{i\mathcal{H}_0(t-\tau_0)}[\hat{V}^{(\dagger)},\cdot]e^{-i\mathcal{H}_0(t-\tau_0)}, \tag{8}$$

where α^s_p indicates whether the positive or negative frequency part of the pth pulse appears in the sequence s and the upper index s_p denotes whether the interaction is carried out via $\hat{V}$ or $\hat{V}^{\dagger}$, respectively. The eight combinations for $\boldsymbol{k}_s$ together with the corresponding sequences are specified in Table I, where we follow the notation given by Mukamel *et al.* [31], extended by the opposite vectors $\boldsymbol{k}_{\text{V}} = -\boldsymbol{k}_{\text{I}}$, $\boldsymbol{k}_{\text{VI}} = -\boldsymbol{k}_{\text{II}}$, $\boldsymbol{k}_{\text{VII}} = -\boldsymbol{k}_{\text{III}}$, and $\boldsymbol{k}_{\text{VIII}} = -\boldsymbol{k}_{\text{IV}}$. According to the macroscopic phase-matching condition [5], depicted in Fig. 1, each term in $\mathcal{P}^{(3)}_s$ contributes to the radiated field $E_{\text{rad}}(\boldsymbol{r},t) = \mathcal{E}_{\text{rad}}(\boldsymbol{r},t) + \mathcal{E}^*_{\text{rad}}(\boldsymbol{r},t)$ according to

$$\mathcal{E}_{\text{rad}}(\boldsymbol{r},t) \propto i \sum_{s=\text{I}}^{\text{VIII}} e^{i\boldsymbol{k}_s\boldsymbol{r}}\mathcal{P}^{(3)}_s(t), \tag{9}$$

TABLE I. Following Eq. (9), each signal emission direction $\boldsymbol{k}_s$ is uniquely linked with a set of individual quantum paths specified by the pulse frequencies $\alpha^s_p\,\omega_p$ and induced transitions $\mathcal{V}_I^{s_p}$. Thus related signals, created by $\mathcal{P}^{(3)}_s$, can only appear if the required elements of ρ are nonzero at the first pulse arrival time τ_1.

s	$\boldsymbol{k}_s$	$(\alpha^s_1,\alpha^s_2,\alpha^s_3)$	$(\mathcal{V}_I^{s_3},\mathcal{V}_I^{s_2},\mathcal{V}_I^{s_1})$	$\mathcal{P}^{(3)}_s(t) \propto$
I	$-\boldsymbol{k}_1+\boldsymbol{k}_2+\boldsymbol{k}_3$	$(+1,-1,-1)$	$(\mathcal{V}_I^{\dagger},\mathcal{V}_I^{\dagger},\mathcal{V}_I)$	$\rho_{n,n}(\tau_1)$
II	$\boldsymbol{k}_1-\boldsymbol{k}_2+\boldsymbol{k}_3$	$(-1,+1,-1)$	$(\mathcal{V}_I^{\dagger},\mathcal{V}_I,\mathcal{V}_I^{\dagger})$	$\rho_{n,n}(\tau_1)$
III	$\boldsymbol{k}_1+\boldsymbol{k}_2-\boldsymbol{k}_3$	$(-1,-1,+1)$	$(\mathcal{V}_I,\mathcal{V}_I^{\dagger},\mathcal{V}_I^{\dagger})$	$\rho_{n,n}(\tau_1)$
IV	$\boldsymbol{k}_1+\boldsymbol{k}_2+\boldsymbol{k}_3$	$(-1,-1,-1)$	$(\mathcal{V}_I^{\dagger},\mathcal{V}_I^{\dagger},\mathcal{V}_I^{\dagger})$	$\rho_{n,n+2}(\tau_1)$
V	$\boldsymbol{k}_1-\boldsymbol{k}_2-\boldsymbol{k}_3$	$(-1,+1,+1)$	$(\mathcal{V}_I,\mathcal{V}_I,\mathcal{V}_I^{\dagger})$	$\rho_{n+2,n}(\tau_1)$
VI	$-\boldsymbol{k}_1+\boldsymbol{k}_2-\boldsymbol{k}_3$	$(+1,-1,+1)$	$(\mathcal{V}_I,\mathcal{V}_I^{\dagger},\mathcal{V}_I)$	$\rho_{n+2,n}(\tau_1)$
VII	$-\boldsymbol{k}_1-\boldsymbol{k}_2+\boldsymbol{k}_3$	$(+1,+1,-1)$	$(\mathcal{V}_I^{\dagger},\mathcal{V}_I,\mathcal{V}_I)$	$\rho_{n+2,n}(\tau_1)$
VIII	$-\boldsymbol{k}_1-\boldsymbol{k}_2-\boldsymbol{k}_3$	$(+1,+1,+1)$	$(\mathcal{V}_I,\mathcal{V}_I,\mathcal{V}_I)$	$\rho_{n+4,n}(\tau_1)$

and therefore exclusively in the respective direction of its $\boldsymbol{k}_s$. Hence emission occurs in directions $\boldsymbol{k}_s$, only if the related $\mathcal{P}_s^{(3)}(t)$ is nonzero, which typically depends on the initial state.

B. Analysis of the emission from a nonequilibrium initial state

The results presented below are obtained by numerically solving Eq. (7) using realistic pulses, as detailed in the next section. However, to get a deeper insight into the mechanism, and to develop general selection rules for emission in all directions, we proceed by considering the semi-impulsive limit $\varepsilon_p(t) \propto \delta(t)$ [32,33]. The third-order signal, Eq. (7), is then proportional to

$$\mathcal{P}_s^{(3)}(t) \propto \mathrm{Tr}\{\hat{V}_I(t)\mathcal{V}_I^{s_3}(\tau_3)\mathcal{V}_I^{s_2}(\tau_2)\mathcal{V}_I^{s_1}(\tau_1)\rho(\tau_0)\}. \qquad (10)$$

Here, each polarization contribution $\mathcal{P}_s^{(3)}$ is composed of eight terms due to the embedded three commutators arising from the superoperators $\mathcal{V}_I^{(\dagger)}$. Hence, for each nonzero element of the initial density matrix $\rho(\tau_0)$ one obtains eight individual quantum paths, which can be represented by double-sided Feynman diagrams. One of these eight fundamental paths is illustrated in Fig. 2 for directions $\boldsymbol{k}_{\mathrm{I}}$ (left) and $\boldsymbol{k}_{\mathrm{V}}$ (right). In the case where the initial density matrix is entirely described by the ground state, i.e., $\rho(\tau_0) = |0\rangle\langle 0|$, the number of nonvanishing paths is reduced to three for $\mathcal{P}_{\mathrm{I}}^{(3)}$, three for $\mathcal{P}_{\mathrm{II}}^{(3)}$, and two for $\mathcal{P}_{\mathrm{III}}^{(3)}$, which have been extensively discussed in literature (see, e.g., Refs. [34,35]), whereas the signals of $\mathcal{P}_{\{\mathrm{IV},\ldots,\mathrm{VIII}\}}^{(3)}$ vanish entirely.

However, if $\rho(\tau_0)$ contains higher populations and nonvanishing coherences, as it is the case for nonequilibrium situations, more quantum paths contribute and more general selection rules apply. If we denote by $\delta = m - n$ the distance of a matrix element $\rho_{m,n}$ from the main diagonal, we see that the action of $\mathcal{V}_I^{\dagger}$ generates matrix elements with $\delta' = \delta + 1$, whereas the action of $\mathcal{V}_I$ generates elements with $\delta' = \delta - 1$. For $\mathcal{P}_s^{(3)}(t)$ to be nonzero, one requires that $\mathcal{V}_I^{s_3}\mathcal{V}_I^{s_2}\mathcal{V}_I^{s_1}\rho(\tau_0)$ leads to matrix elements with $\delta = 1$ after τ_3, i. e., entries in the first lower off-diagonal. Applying successively the transition operators on $\rho(\tau_0)$ yields selection rules for the required elements of the initial density matrix at the arrival time of the first pulse τ_1, leading to the right column in Table I. We see that each signal $\mathcal{P}_s^{(3)}$ in a specific direction $\boldsymbol{k}_s$ is induced exclusively by entries from a single diagonal of the initial density matrix, i.e., the main diagonal for $s = \{\mathrm{I},\mathrm{II},\mathrm{III}\}$, the second off-diagonal for $s = \{\mathrm{IV},\mathrm{V},\mathrm{VI},\mathrm{VII}\}$, and the fourth off-diagonal for $s = \mathrm{VIII}$. To summarize, these rules not only provide the well-known emission signals I to III, where only populations of $\rho(\tau_1)$ are relevant, but also radiative signals in the opposite directions, if $\rho(\tau_1)$ has coherences. In particular, we see that $|n+2\rangle\langle n|$ coherences yield radiative signals in the unconventional directions IV to VII.

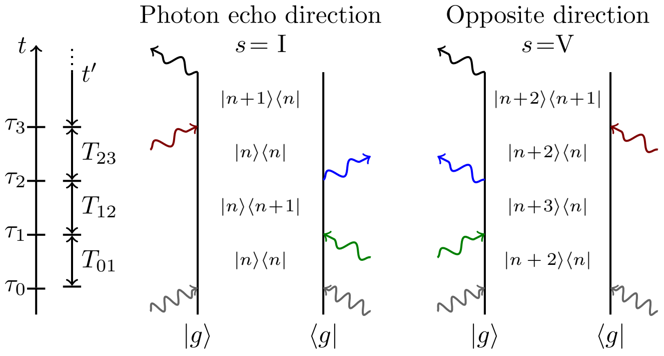

FIG. 2. (Color online) Double-sided Feynman diagrams illustrating one out of eight quantum paths for each initial matrix element $\rho_{m,n}(\tau_0)$ contributing to the photon-echo signal $\mathcal{P}_{\mathrm{I}}^{(3)}$ (left) and the $\mathcal{P}_{\mathrm{V}}^{(3)}$ signal in the opposite direction (right), respectively. The state of the system prior to the UV excitation is denoted by $|g\rangle$.

This is the central result of this paper, and will be numerically confirmed below, by considering a model based on recent experiments [36] describing the vibrational motion of UV-photolyzed carbon monoxide in a hemeprotein environment.

III. NUMERICAL SIMULATION

To compute the contribution of the third-order polarization leading to an emission in the direction $\boldsymbol{k}_s$, we rewrite Eq. (7) by switching back to the Schrödinger representation

$$\mathcal{P}_s^{(3)}(t) = \mathrm{Tr}\big\{\hat{V}\rho_s^{(3)}(t)\big\}, \qquad (11)$$

where the third-order density matrix can be obtained by numerically solving the set of coupled quantum Liouville equations

$$\begin{aligned}
\dot{\rho}_s^{(3)} &= -i\mathcal{H}_0\rho_s^{(3)} + i\varepsilon_3(t-\tau_3)e^{i\alpha_3^s\omega_3(t-\tau_3)}\mathcal{V}^{s_3}\rho_s^{(2)},\\
\dot{\rho}_s^{(2)} &= -i\mathcal{H}_0\rho_s^{(2)} + i\varepsilon_2(t-\tau_2)e^{i\alpha_2^s\omega_2(t-\tau_2)}\mathcal{V}^{s_2}\rho_s^{(1)},\\
\dot{\rho}_s^{(1)} &= -i\mathcal{H}_0\rho_s^{(1)} + i\varepsilon_1(t-\tau_1)e^{i\alpha_1^s\omega_1(t-\tau_1)}\mathcal{V}^{s_1}\rho^{(0)},\\
\dot{\rho}^{(0)} &= -i\mathcal{H}_0\rho^{(0)}, \qquad (12)
\end{aligned}$$

with initial conditions $\rho_s^{(3)}(\tau_0) = \rho_s^{(2)}(\tau_0) = \rho_s^{(1)}(\tau_0) = 0$ and $\rho^{(0)}(\tau_0) = \rho(\tau_0)$. We assume that the sudden photolysis at τ_0 leads to a CO fragment which can be described by a pure state

$$\rho^{(0)}(\tau_0) = |\Psi(\tau_0)\rangle\langle\Psi(\tau_0)|, \qquad (13)$$

with $|\Psi(\tau_0)\rangle = \sum_n c_n(\tau_0)|n\rangle$ and $c_0(\tau_0) = \sqrt{0.85}$, $c_1(\tau_0) = \sqrt{0.13}$, and $c_2(\tau_0) = \sqrt{0.02}$, reproducing the populations found in Ref. [36].

Since the CO molecule inside the protein cavity is subject to decoherence, we add a phenomenological state-dependent exponential damping of the coherences $\rho_{m,n}$ with time constants $\gamma_{m,n} = \gamma_{n,m}$. Since energy relaxation is considered to be weak on this time scale, it has not been included numerically. All numerical values of the parameters used in the simulation are summarized in Appendix B. The differential equations (12) are solved, using a fourth-order Runge-Kutta algorithm [37].

The polarization, determined via Eq. (11), is the central quantity to evaluate different spectra, as detailed below. Note that $\mathcal{P}_s^{(3)}(t)$ is also a function of the delay time between the UV pump pulse and the three IR pulses, as well as of the delay times between the three IR pulses.

IV. RESULTS AND DISCUSSION

A. Four-wave-mixing signals in directions $\boldsymbol{k}_{\mathrm{I}}$ and $\boldsymbol{k}_{\mathrm{V}}$

The model, introduced in the previous section, is inspired by recent experiments [36], where a first UV pulse separates the CO molecule from its ligand, which is subsequently analyzed by an IR pulse. If instead of a single probing IR pulse, a 2D-IR pulse sequence is employed, as depicted in Fig. 1, possible vibrational coherences that may stem from the ultrafast dissociation dynamics could in principle be detected, and their decay directly measured in the time domain.

In a heterodyne detection scheme with a spectrometer placed in a specific direction $\boldsymbol{k}_s$, the measured signal provides access to the spectral function [38,39]

$$S_s(\omega) \propto \int dt\, i\mathcal{P}_s^{(3)}(t)e^{i\omega t}. \tag{14}$$

Our simulations of such experiments show that not only the presence of coherences at time τ_1 manifests itself in a measurable signal along unconventional directions, but also that the decay of these coherences can be directly monitored by delaying the three IR pulses with respect to the UV pump pulse.

To this end, we calculate the integrated signal

$$\tilde{S}_s(T_{01}) = \int |S_s(\omega)| d\omega \tag{15}$$

as a function of the UV-IR delay time $T_{01} = \tau_1 - \tau_0$ for two directions, $s = \mathrm{I}$ (photon echo direction) and $s = \mathrm{V}$ (opposite direction). The results are shown in Fig. 3. According to Table I, the signal determined by the polarization $\mathcal{P}_{\mathrm{I}}^{(3)}$ is proportional to populations $\rho_{n,n}(\tau_1)$ and, thus, no T_{01} dependency can be found (blue circles). On the contrary, in the opposite $\boldsymbol{k}_{\mathrm{V}}$ direction (red crosses), we see an overall signal intensity, which is entirely determined by the $\rho_{n+2,n}$ coherences, and hence vanishes as the coherences die out. The observed signal extinction directly reflects the exponential coherence decay of $\rho_{2,0}(\tau_1)$ (solid line). The same holds also for the signals emitted in the unconventional directions $\boldsymbol{k}_{\mathrm{VI}}$ and $\boldsymbol{k}_{\mathrm{VII}}$, although showing different overall intensities based on their individual quantum paths. Through these detection schemes using unconventional directions, one can thus directly probe the coherence decay.

Since populations in the initial state do not yield a signal contribution in these directions, the coherence measurement is background free. In the case that more than one $\rho_{n+2,n}$ elements are nonzero at τ_1, state resolution can in general be achieved by evaluating spectral peaks separately by using proper limits of integration in Eq. (15). However, more advanced techniques, which are addressed in the next section, might be helpful to further separate individual quantum paths. In the particular setup used for the simulation in Fig. 3, only T_{01}, i.e., the onset of the three detecting pulses, is scanned. The interpulse separation between the three detecting pulses T_{12} and T_{23} is kept fixed. Inspection of the Feynman diagram showing the origin of the emission in the $\boldsymbol{k}_{\mathrm{V}}$ direction (Fig. 2, right) reveals that it depends on coherence evolution $|n+3\rangle\langle n|$ between the first and the second IR pulse. While in practice this might lead to a strong overall damping of the signal, this property can also be exploited to yield information on this three-quantum coherence, in analogy with recent approaches [40–42]. This can be achieved by additionally varying the time delay between the first and the second IR pulse, T_{12}, giving rise to two-dimensional spectra. This approach is analyzed in the next section.

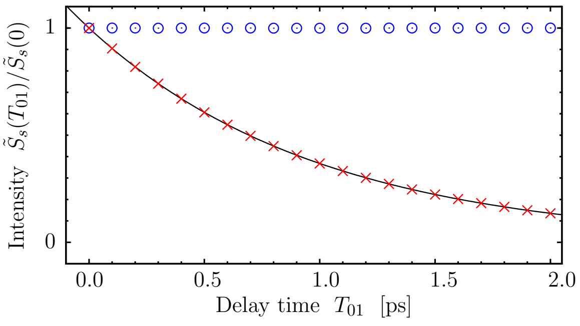

FIG. 3. (Color online) Integrated signal $\tilde{S}_s(T_{01}), s = \{\mathrm{I,V}\}$, over the UV-IR delay time $T_{01} = \tau_1 - \tau_0$ for signals emitted in the directions $\boldsymbol{k}_{\mathrm{I}}$ (blue circles) and $\boldsymbol{k}_{\mathrm{V}}$ (red crosses). While the $\boldsymbol{k}_{\mathrm{I}}$ signal is independent of coherence decay between τ_0 and τ_1, the signal in the opposite direction, $\boldsymbol{k}_{\mathrm{V}}$, fades reflecting the decay of $|\rho_{2,0}(\tau_1)|$, taken to be exponential with time constant $\gamma_{2,0}^{-1} = 1.0$ ps (solid line).

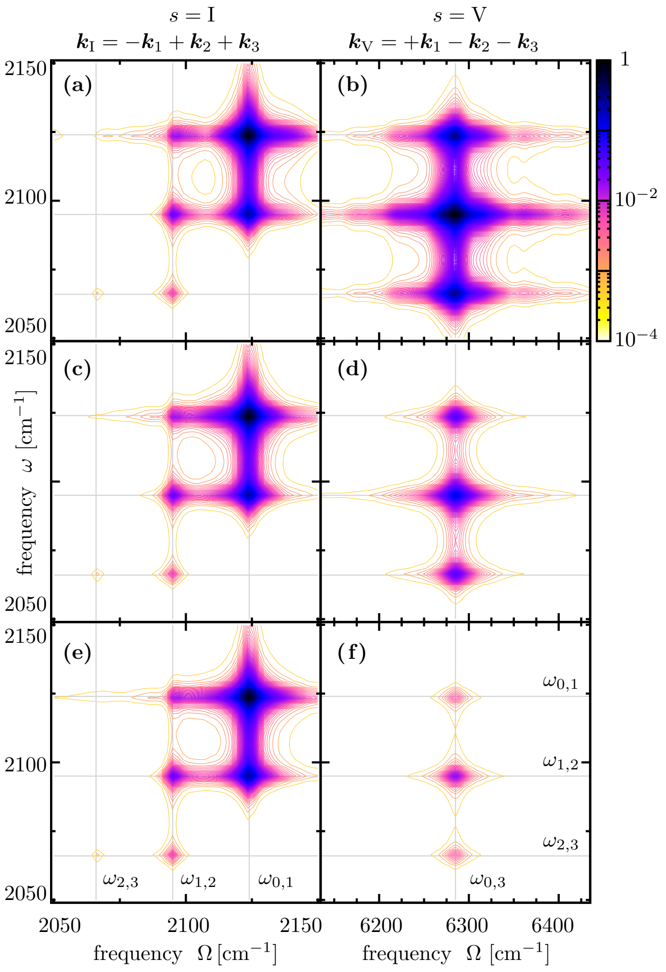

FIG. 4. (Color online) 2D spectra $|\sigma_{\mathrm{I}}(\omega,\Omega)|^2$ in $\boldsymbol{k}_{\mathrm{I}}$ direction (left) and $|\sigma_{\mathrm{V}}(\omega,\Omega)|^2$ in $\boldsymbol{k}_{\mathrm{V}} = -\boldsymbol{k}_{\mathrm{I}}$ direction (right) for UV-IR delay times $T_{01} = 0$ ps (a), (b), 1 ps (c), (d), and 2 ps (e), (f). While the intensities show the same T_{01} dependence as in Fig. 3, the linewidths provide further, state-resolved information about dephasing processes addressing the 3Q elements of the density matrix, $\rho_{n+3,n}$.

B. Nonequilibrium 2D-IR spectroscopy with detection in directions $\boldsymbol{k}_{\mathrm{I}}$ and $\boldsymbol{k}_{\mathrm{V}}$

As stated above, additional information can be obtained by not only scanning T_{01} but also T_{12}. As can be seen from the Feynman diagram (Fig. 2), the signal emission relies on a three-quantum coherence evolution between the first and second IR pulse. By modulating this second delay time T_{12}, as defined in Fig. 1, one obtains a 2D spectrum via a second Fourier transform

$$\sigma_s(\omega,\Omega) \propto \int dT_{12} S_s(\omega) e^{-i\Omega T_{12}}. \tag{16}$$

In Fig. 4 the absolute square of the 2D spectra for the $\boldsymbol{k}_{\mathrm{I}}$ (left) and $\boldsymbol{k}_{\mathrm{V}} = -\boldsymbol{k}_{\mathrm{I}}$ directions (right) are shown for different UV-IR delay times T_{01}. First, not surprisingly, we see that one finds the same overall intensity damping as a function of T_{01} as in Fig. 3, reflecting the coherence decay of $\rho_{n+2,n}$ within this time span. For the conventional detection in $\boldsymbol{k}_{\mathrm{I}}$ direction, the signal does not show this decay, since it is proportional to populations, which we assumed to show a negligible decay on this time scale. The second axis, Ω, provides further state-resolved information about the system dynamics by peak positions and linewidths [43–45]. In particular, quantum paths leading to an emission signal are separated by their intermediate states between times τ_1 and τ_2. While in $\boldsymbol{k}_{\mathrm{I}}$ direction both axes show peaks at nearest-neighbor-state transition energies $\omega_{n,n+1} = \epsilon_{n+1} - \epsilon_n$ with linewidths determined by $\gamma_{n,n+1}$, the unconventional $\boldsymbol{k}_{\mathrm{V}}$ direction reveals along the Ω axis energy differences $\omega_{0,3}$ of eigenstates three quanta apart, which causes a broadened signal according to the stronger damping by $\gamma_{n,n+3}$. As stated above, this can be understood from the Feynman diagrams shown in Fig. 2 (right). In analogy to two-quantum (2Q) 2D-IR spectroscopy [40], one could refer to this spectroscopic feature as three-quantum (3Q) 2D-IR spectroscopy. This particular feature will be further analyzed in the next section.

C. Nonequilibrium 2Q and 3Q 2D-IR spectra in other phase-matching directions

The presented results on initial $\rho_{n+2,n}$ coherences leading to signal emission in a direction opposite to the conventional photon-echo one can be generalized to other nonconventional directions. Using Table I, the third-order polarization can be analyzed according to Eq. (10). Due to the nested commutators appearing in Eq. (10), for each direction $s = \{\mathrm{I},\ldots,\mathrm{VIII}\}$, eight distinct quantum paths exist, which can be visualized by corresponding Feynman diagrams, following the standard rules [5]. This yields information on which coherences are involved in the evolution between the different detection pulses. This analysis reveals that a T_{12} modulation yields 3Q signals only for the unconventional directions $\boldsymbol{k}_{\mathrm{V}}$ and $\boldsymbol{k}_{\mathrm{VIII}}$. On the other hand, modulating the T_{23} delay, provides 2Q signals for detection directions $\boldsymbol{k}_{\mathrm{V}}$, $\boldsymbol{k}_{\mathrm{VI}}$, and $\boldsymbol{k}_{\mathrm{VIII}}$. The latter techniques are hence similar to conventional methods based on $\boldsymbol{k}_{\mathrm{III}}$ detection schemes [40–42], but in contrast to those, they rely on the presence of coherences in the initial nonequilibrium state. Figure 5 shows 2D spectra for the directions $\boldsymbol{k}_{\mathrm{V}}$, $\boldsymbol{k}_{\mathrm{VI}}$, and $\boldsymbol{k}_{\mathrm{VII}}$ revealing the effect of multiquantum coherences during T_{12} and T_{23} on the Ω axis. For the directions $\boldsymbol{k}_{\mathrm{VI}}$ and $\boldsymbol{k}_{\mathrm{VII}}$ one of the eight fundamental quantum paths is depicted in Fig. 6 as an illustration.

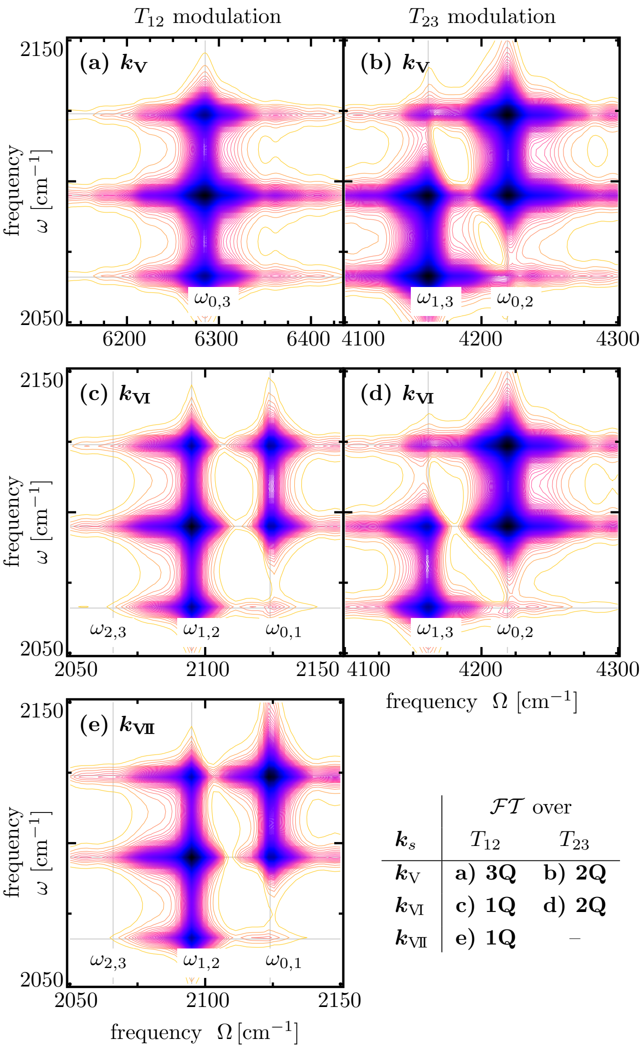

$\boldsymbol{k}_s$	$\mathcal{FT}$ over T_{12}	$\mathcal{FT}$ over T_{23}
$\boldsymbol{k}_{\mathrm{V}}$	**a) 3Q**	**b) 2Q**
$\boldsymbol{k}_{\mathrm{VI}}$	**c) 1Q**	**d) 2Q**
$\boldsymbol{k}_{\mathrm{VII}}$	**e) 1Q**	–

FIG. 5. (Color online) 2D spectra $|\sigma_s(\omega,\Omega)|^2$ showing multiquantum coherences in $\boldsymbol{k}_{\mathrm{V}}$ (upper panel), $\boldsymbol{k}_{\mathrm{VI}}$ (middle panel), and $\boldsymbol{k}_{\mathrm{VII}}$ direction (lower panel), obtained by modulating the IR pulse delay T_{12} (left column), and T_{23} (right column), respectively. The UV-IR delay is kept fixed at $T_{01} = 0$ ps. Peaks along the Ω axis reveal different coherences depending on the individual quantum paths of each direction of emission and modulated pulse delay; see Figs. 2 and 6. Color scheme as defined in Fig. 4.

Finally, we want to add, that in the case of short coherence lifetimes, signal intensities might be weak. In this case, a detecting direction should be chosen based on quantum paths, which are less exposed to environmental dephasing processes during the detection sequence. Given the typical case, that higher quantum coherences decay faster than nearest-neighbor coherences, the most advantageous unconventional direction—from this practical point of view—is $\boldsymbol{k}_{\mathrm{VII}}$, since after the first IR pulse, the loss of signal intensity due to dephasing is determined only by nearest-neighbor-state decoherence. This structure can be understood by examining the corresponding Feynman diagrams shown in Fig. 6 (right).

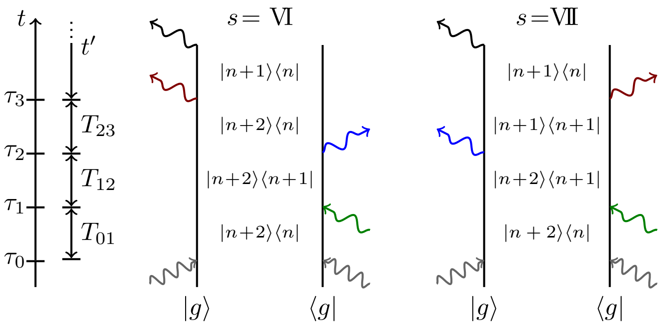

FIG. 6. (Color online) Double-sided Feynman diagrams illustrating one out of eight quantum paths for each initial matrix element $\rho_{n+2,n}(\tau_0)$ contributing to the polarizations $\mathcal{P}^{(3)}_{\text{VI}}$ (left) and $\mathcal{P}^{(3)}_{\text{VII}}$ (right). The emission in the $\boldsymbol{k}_{\text{VII}}$ direction relies on lower quantum coherences and is therefore expected to be of higher intensity.

V. CONCLUSION

In this work, we considered a system in a nonequilibrium state, which is probed by an FWM-IR-pulse sequence. We have shown that the presence of vibrational coherences causes signal emission in directions opposite to the ones used conventionally. These signals are directly proportional to off-diagonal elements of the nonequilibrium density matrix. Delaying the probe sequence allows a direct, background-free measurement of coherences with temporal resolution. In addition, varying the IR pulse delays with respect to each other yields 2D spectra, determined by the system dynamics during these delay times. Thus signals are spectrally separated by their individual quantum paths, providing further state-resolved information of both energies and decay properties of one-, two-, and three-quantum states, depending on the detection direction. We believe that this 2D spectroscopy technique will help to shed light on the role coherences play in various biochemical processes and that the availability of their time-resolved measurement also paves the way to utilize coherence decays as a sensitive probe for an in-depth analysis of environmental influences.

ACKNOWLEDGMENTS

A.S. gratefully acknowledges financial support by the German Research Foundation (DFG) [SCHU 2965/1-1]. This work is partially funded by the Agence Nationale de la Recherche (ANR) within the PROCONTROL project [ANR-11-BS04-0027]. Computational facilities were provided by CALMIP (Toulouse).

APPENDIX A: NONEQUILIBRIUM STATE PREPARATION THROUGH UV INTERACTION

The results presented in this paper are general, and hold for any triggering mechanism leading to a spatially homogeneous distribution of samples in a nonequilibrium quantum system. Such a situation is present for vibrational coherences realized by a nuclear wave packet created in an electronically excited state by a UV pulse absorption. If, as in many pump-probe experiments, the exciting UV pulse is short compared to the vibrations, but long with respect to electronic transitions, the pulse interaction leads to a coherent excitation of several vibrational levels within the electronically excited state. In particular, guided by recent experiments, we detail here the special case where a UV pulse dissociates a CO molecule from a hemeprotein [36]. To this end, we consider an extended molecular entity, described by the total Hamiltonian $\hat{H}_t$, which includes not only the CO stretch to be analyzed, but also additional nuclear and electronic degrees of freedom, collectively denoted by $\boldsymbol{R}$. The UV pulse is taken to be $E_{UV}(\boldsymbol{r},t) = \mathcal{E}_0(\boldsymbol{r},t) + \mathcal{E}_0^*(\boldsymbol{r},t)$ with $\mathcal{E}_0(\boldsymbol{r},t) = \varepsilon_0(t-\tau_0)e^{i\boldsymbol{k}_0\boldsymbol{r}}e^{-i\omega_0(t-\tau_0)}$, where $\boldsymbol{k}_0$, ω_0, τ_0, and $\varepsilon_0(t)$ are the wave-vector, frequency, center, and envelope. Its interaction with the extended Hamiltonian is described by second-order perturbation theory. The second-order correction term to the density matrix of the extended system, ρ_t, located at $\boldsymbol{r}$, is thus given by

$$\rho_t^{(2)}(\boldsymbol{r},t_0) = \int_{t_i}^{t_0} dt_0' \int_{t_i}^{t_0'} dt_0'' e^{-i\mathcal{H}_t(t_0-t_0')}\mathcal{W}_0(\boldsymbol{r},t_0') \times e^{-i\mathcal{H}_t(t_0'-t_0'')}\mathcal{W}_0(\boldsymbol{r},t_0'')e^{-i\mathcal{H}_t(t_0''-t_i)}\rho_t(t_i), \quad \text{(A1)}$$

where we assume at the initial time t_i a spatially uniform distribution of molecular entities in their ground state. In this expression, $\mathcal{H}_t$ is the Liouville operator corresponding to $\hat{H}_t$, defined by $\mathcal{H}_t = [\hat{H}_t, \cdot\ ]$, and $\mathcal{W}_0$ is the Liouville operator corresponding to the interaction operator

$$\hat{W}_0(\boldsymbol{r},t) = -\hat{\mu}_e(\mathcal{E}_0^*(\boldsymbol{r},t) + \mathcal{E}_0(\boldsymbol{r},t)), \quad \text{(A2)}$$

with $\hat{\mu}_e$ being the electronic transition dipole operator. This UV interaction will not only lead to the above-mentioned excitation of vibrational wave packets on the excited electronic states, but also to electronic coherences and to vibrational coherences (wave packets) in the electronic ground state. The corresponding terms are found by developing the commutators in Eq. (A1). If we assume that the vibrational motion in the ground state is sufficiently different from the vibrational motion in the electronically excited state to be spectrally separated, it is sufficient to consider the excited-state wave packet only. Among the four terms appearing by developing the commutators in Eq. (A1), the excited state wave packet is described by

$$\rho_t^{(2)}(t_0) = \int_{t_i}^{t_0} dt_0' \int_{t_i}^{t_0} dt_0''(\hat{U}(t_0,t_0')\mathcal{E}_0(\boldsymbol{r},t_0')\hat{\mu}_e\hat{U}(t_0',t_i)\rho_t(t_i) \times \hat{U}(t_i,t_0'')\mathcal{E}_0^*(\boldsymbol{r},t_0'')\hat{\mu}_e\hat{U}(t_0'',t_0)), \quad \text{(A3)}$$

where $\hat{U}(t_2,t_1) = \exp(-i\hat{H}_t(t_2-t_1))$ is the propagator corresponding to $\hat{H}_t$. Note that, due to the appearance of both $\mathcal{E}_0(\boldsymbol{r},t_0')$ and $\mathcal{E}_0^*(\boldsymbol{r},t_0')$, the spatial phase dependence to the excitation pulse vanishes, leading to a spatially uniform distribution of excited-state molecules. If the excited-state motion leads to the dissociation of a CO fragment, its internal vibrational state is obtained by tracing out all other degrees of freedom, collectively denoted by $\boldsymbol{R}$:

$$\rho(t_0) = \text{Tr}_R\{\rho_t^{(2)}(t_0)\}. \quad \text{(A4)}$$

This provides the initial density matrix in the vibrational subspace, which, depending on the dissociation dynamics, might contain vibrational coherences, which can be detected by the IR pulse sequence considered in this work. The main point of this demonstration is to show that this pulse interaction leads to a spatially homogeneous sample of vibrationally excited molecules, serving as initial state in Eq. (5).

APPENDIX B: SIMULATION PARAMETERS

The vibrational eigenstates of the CO in its protein environment are modeled by $\epsilon_n = \bar{\epsilon}(n+1/2) - \delta\bar{\epsilon}(n+1/2)^2$, where $\bar{\epsilon} = 2153$ cm^{-1} and $\delta\bar{\epsilon} = 14.5$ cm^{-1}, reproducing the experimental findings in Ref. [36]. All laser pulses have a sine squared envelope function with a temporal width of 30 fs. The central pulse frequency ω_p is 2000 cm^{-1} for all IR pulses. The UV-IR delay time T_{01} is set to different values between 0 and 2 ps, as indicated in Fig. 3, 4, and 5. While the delay between the first and the second IR pulse T_{12} is varied from 0.075 ps up to 16.459 ps in steps of $\Delta T_{12} = 1$ fs (2^{14} steps), the pulses 2 and 3 are separated from each other by a fixed shift of $T_{23} = 75$ fs—and vice versa in the case that T_{23} is modulated, while T_{12} is kept fixed. Dephasing is simulated by a phenomenological exponential decay of coherences between vibrational states $|m\rangle$ and $|n\rangle$ with time constants $\gamma_{m,n} = \gamma_{n,m}$, which are taken to be $\gamma_{n,n+1}^{-1} = 3000$ fs, $\gamma_{n,n+2}^{-1} = 1000$ fs, and $\gamma_{n,n+3}^{-1} = 600$ fs, guided by Ehrenfest-MD simulations. After the third pulse vanishes, the polarizations $\mathcal{P}_s^{(3)}(t,T_{12})$ and $\mathcal{P}_s^{(3)}(t,T_{23})$, respectively, are stored over 2^{14} time steps ($dt = 1$ fs). A 2D Fourier transform [46] of $\mathcal{P}_s^{(3)}(t,T_{12})$ [$\mathcal{P}_s^{(3)}(t,T_{23})$] gives rise to a complex-valued spectral function.

[1] W. P. Aue, E. Bartholdi, and R. R. Ernst, J. Chem. Phys. **64**, 2229 (1976).
[2] L. Lepetit and M. Joffre, Opt. Lett. **21**, 564 (1996).
[3] P. Hamm, M. Lim, and R. M. Hochstrasser, Phys. Rev. Lett. **81**, 5326 (1998).
[4] J. D. Hybl, A. W. Albrecht, S. M. Gallagher Faeder, and D. M. Jonas, Chem. Phys. Lett. **297**, 307 (1998).
[5] S. Mukamel, *Principles of Nonlinear Optical Spectroscopy*, Oxford Series in Optical and Imaging Sciences (Oxford University Press, Oxford, 1995).
[6] M. Cho, *Two-Dimensional Optical Spectroscopy* (CRC Press, Boca Raton, FL, 2009).
[7] P. Hamm and M. Zanni, *Concepts and Methods of 2D Infrared Spectroscopy* (Cambridge University Press, Cambridge, UK, 2011).
[8] M. Martin and J. Hynes, *Femtochemistry and Femtobiology: Ultrafast Events in Molecular Science* (Elsevier Science, Amsterdam, 2004).
[9] M. Cho, T. Brixner, I. Stiopkin, H. Vaswani, and G. R. Fleming, J. Chin. Chem. Soc. **53**, 15 (2006).
[10] G. S. Engel, T. R. Calhoun, E. L. Read, T.-K. Ahn, T. Mančal, Y.-C. Cheng, R. E. Blankenship, and G. R. Fleming, Nature (London) **446**, 782 (2007).
[11] Y. S. Kim and R. M. Hochstrasser, J. Phys. Chem. B **113**, 8231 (2009).
[12] *Ultrafast Infrared Vibrational Spectroscopy*, edited by M. Fayer (Taylor & Francis, London, 2013).
[13] J. Bredenbeck, J. Helbing, and P. Hamm, Phys. Rev. Lett. **95**, 083201 (2005).
[14] P. Hamm, J. Chem. Phys. **124**, 124506 (2006).
[15] H. S. Chung, Z. Ganim, K. C. Jones, and A. Tokmakoff, Proc. Natl. Acad. Sci. USA **104**, 14237 (2007).
[16] J. Bredenbeck, J. Helbing, C. Kolano, and P. Hamm, ChemPhysChem **8**, 1747 (2007).
[17] C. R. Baiz, M. J. Nee, R. McCanne, and K. J. Kubarych, Opt. Lett. **33**, 2533 (2008).
[18] M. S. Lynch, K. M. Slenkamp, M. Cheng, and M. Khalil, J. Phys. Chem. A **116**, 7023 (2012).
[19] M. S. Lynch, K. M. Slenkamp, and M. Khalil, J. Chem. Phys. **136**, 241101 (2012).
[20] J. S. Briggs and A. Eisfeld, Phys. Rev. E **83**, 051911 (2011).
[21] G. Ritschel, J. Roden, W. T. Strunz, A. Aspuru-Guzik, and A. Eisfeld, J. Phys. Chem. Lett. **2**, 2912 (2011).
[22] N. Christensson, H. F. Kauffmann, T. Pullerits, and T. Mančal, J. Phys. Chem. B **116**, 7449 (2012).
[23] J. Strümpfer, M. Şener, and K. Schulten, J. Phys. Chem. Lett. **3**, 536 (2012).
[24] N. Lambert, Y.-N. Chen, Y.-C. Cheng, C.-M. Li, G.-Y. Chen, and F. Nori, Nat. Phys. **9**, 10 (2013).
[25] I. Kassal, J. Yuen-Zhou, and S. Rahimi-Keshari, J. Phys. Chem. Lett. **4**, 362 (2013).
[26] R. Tempelaar, F. C. Spano, J. Knoester, and T. l. C. Jansen, J. Phys. Chem. Lett. **5**, 1505 (2014).
[27] J. Albert, M. Falge, M. Keß, J. G. Wehner, P.-P. Zhang, A. Eisfeld, and V. Engel, J. Chem. Phys. **142**, 212440 (2015).
[28] T. V. Tscherbul and P. Brumer, Phys. Chem. Chem. Phys. (2015).
[29] B. K. Agarwalla, K. E. Dorfman, and S. Mukamel, Phys. Rev. A **91**, 052501 (2015).
[30] S. Mukamel and S. Rahav, Adv. At., Mol., Opt. Phys. **59**, 223 (2010).
[31] C. Scheurer and S. Mukamel, J. Chem. Phys. **115**, 4989 (2001).
[32] G. Stock and W. Domcke, Phys. Rev. A **45**, 3032 (1992).
[33] S. Mukamel, A. Piryatinski, and V. Chernyak, Acc. Chem. Res. **32**, 145 (1999).
[34] S. Mukamel and D. Abramavicius, Chem. Rev. **104**, 2073 (2004).
[35] D. Abramavicius, B. Palmieri, D. V. Voronine, F. Šanda, and S. Mukamel, Chem. Rev. **109**, 2350 (2009).
[36] P. Nuernberger, K. F. Lee, A. Bonvalet, L. Bouzhir-Sima, J.-C. Lambry, U. Liebl, M. Joffre, and M. H. Vos, J. Am. Chem. Soc. **133**, 17110 (2011).
[37] E. Hairer, S. P. Nørsett, and G. Wanner, in *Solving Ordinary Differential Equations I*, 2nd ed., edited by R. Bank, R. Graham, W. Hackbusch, J. Stoer, R. Varga, and H. Yserentant, Springer Series in Computational Mathematics Vol. 8 (Springer-Verlag, Berlin, 1993).
[38] W. P. de Boeij, M. S. Pshenichnikov, and D. A. Wiersma, Chem. Phys. Lett. **238**, 1 (1995).
[39] O. Golonzka, M. Khalil, N. Demirdöven, and A. Tokmakoff, J. Chem. Phys. **115**, 10814 (2001).
[40] E. C. Fulmer, P. Mukherjee, A. T. Krummel, and M. T. Zanni, J. Chem. Phys. **120**, 8067 (2004).

[41] N. Christensson, F. Milota, A. Nemeth, I. Pugliesi, E. Riedle, J. Sperling, T. Pullerits, H. F. Kauffmann, and J. Hauer, J. Phys. Chem. Lett. **1**, 3366 (2010).

[42] X. Dai, M. Richter, H. Li, A. D. Bristow, C. Falvo, S. Mukamel, and S. T. Cundiff, Phys. Rev. Lett. **108**, 193201 (2012).

[43] J. Sung and R. J. Silbey, J. Chem. Phys. **115**, 9266 (2001).

[44] N. Demirdöven, M. Khalil, and A. Tokmakoff, Phys. Rev. Lett. **89**, 237401 (2002).

[45] M. Khalil, N. Demirdöven, and A. Tokmakoff, Phys. Rev. Lett. **90**, 047401 (2003).

[46] J. W. Cooley and J. W. Tukey, Math. Comput. **19**, 297 (1965).